Boosting the Edelstein effect of two-dimensional electron gases by ferromagnetic exchange

Gabriel Lazrak,[1] Börge Göbel,[2] Agnès Barthélémy,[1] Ingrid Mertig,[2] Annika Johansson,[3,*] and Manuel Bibes[1,†]

[1]*Laboratoire Albert Fert, CNRS, Thales, Université Paris-Saclay, 91767 Palaiseau, France*

[2]*Institut für Physik, Martin-Luther-Universität, Halle-Wittenberg, 06099 Halle (Saale), Germany*

[3]*Max Planck Institute of Microstructure Physics, Weinberg 2, 06120 Halle (Saale), Germany*

(Received 28 September 2023; revised 19 January 2024; accepted 24 January 2024; published 22 April 2024)

Strontium titanate ($SrTiO_3$) two-dimensional electron gases (2DEGs) have broken spatial inversion symmetry and possess a finite Rashba spin-orbit coupling. This enables the interconversion of charge and spin currents through the direct and inverse Edelstein effects, with record efficiencies at low temperature but more modest effects at room temperature. Here, we show that making these 2DEGs ferromagnetic enhances the conversion efficiency by nearly one order of magnitude. Starting from the experimental band structure of nonmagnetic $SrTiO_3$ 2DEGs, we mimic magnetic exchange coupling by introducing an out-of-plane Zeeman term in a tight-binding model. We then calculate the band structure and spin textures for increasing internal magnetic fields and compute the Edelstein effect using a semiclassical Boltzmann approach. We find that the conversion efficiency first increases strongly with increasing magnetic field, then shows a maximum, and finally decreases. This field dependence is caused by the competition of the exchange coupling with the effective Rashba interaction. While the magnetic field enhances the splitting of band pairs (both in momentum and in spin expectation value), it also weakens the in-plane Rashba-type spin texture. The former mechanism increases the Edelstein effect, and the latter reduces it.

DOI: 10.1103/PhysRevResearch.6.023074

I. INTRODUCTION

Since the discovery of a quasi-two-dimensional electron gas (2DEG) at the interface between the two band insulators $LaAlO_3$ and $SrTiO_3$ (STO) [1], 2DEGs at oxide surfaces and interfaces have attracted a lot of attention due to their very rich physics. Superconductivity [2], magnetism [3,4], gate tunable metal-insulator and superconductor-insulator transitions [5,6], as well as Rashba spin-orbit coupling (SOC) [7] make them also promising for applications [8,9]. Additionally, recent experiments have revealed their unprecedented efficiency for spin to charge current interconversion [10,11], which is key for new devices such as the magnetoelectric spin-orbit (MESO) transistor proposed by Intel for beyond complementary metal-oxide semiconductor computing schemes [12,13]. However, to date, despite much progress the spin-charge conversion efficiency of available materials [14] still falls short of the requirement for operational MESO-based architectures, that require output voltages of at least 100 mV. Estimates using conversion efficiency figures of merit obtained for STO yield possible output voltages in the 10-mV range [11], although the actual room-temperature operation of MESO-type devices based on STO remains elusive [15]. This points to the critical need for systems with enhanced spin-charge conversion efficiencies.

As described in more detail in Refs. [10,11], in STO 2DEGs, the inversion symmetry breaking at the interface results in a built-in electric field perpendicular to the interface and thus an additional effective term in the Hamiltonian of the system, the Rashba term, that lifts the spin degeneracy and locks the spin and momentum degrees of freedom. In the simplest case of linear Rashba coupling, this results in two slightly different Fermi contours with opposite spin chiralities. In the inverse Edelstein effect, the injection of a pure spin current perpendicular to the interface can be interpreted as a shift of the two contours in opposite directions to accommodate the spin accumulation. This slight nonequivalence leads to the generation of a charge current within the 2DEG (spin-charge conversion). Its reciprocal effect, the direct Edelstein effect, is achieved by applying an electric field that leads to a reoccupation of states, often visualized as a shift of both Fermi contours in the same direction. This results in a net spin density generation that can diffuse as a pure spin current into an adjacent material (charge-spin conversion).

Recently, possibilities to further enlarge or control the functionalities of STO 2DEGs have emerged. One approach relies on making the 2DEG ferroelectric by exploiting the large electric-field- or Ca-doping-induced ferroelectric character in STO [16,17], thereby enabling a nonvolatile control of the transport and spin-charge interconversion properties. Another is by inducing spin polarization in the 2DEG by depositing a magnetic layer on top of STO [18–24]. Combining both strategies, multiferroic 2DEGs have been realized [25],

*annika.johansson@mpi-halle.mpg.de
†manuel.bibes@cnrs-thales.fr

opening an avenue for ferroelectrically controllable chiral spin textures in 2DEGs and providing a new playground for nonvolatile spin-orbitronics and nonreciprocal physics.

Here, by combining a tight-binding Hamiltonian and a semiclassical Boltzmann approach, we predict that introducing ferromagnetism in STO 2DEGs can enhance the spin-charge interconversion efficiency by nearly one order of magnitude. The nonmonotonic dependence of this efficiency with the amplitude of the induced magnetization is explained by the interplay between magnetic exchange coupling and Rashba-like spin-orbit coupling, that causes a subband splitting, as well as a magnetically induced out-of-plane spin polarization. This enhancement is of great promise to obtain spin-charge interconversion large enough for room temperature applications.

II. BAND STRUCTURE AND SPIN TEXTURE

We use an effective eight-band tight-binding model introduced in Refs. [11,26–28] in order to model the t_{2g} electronic states which are relevant for the formation of the 2DEG at STO interfaces. Our model includes two d_{xy} orbitals as well as one d_{yz} and one d_{zx} orbital and has been demonstrated to appropriately approximate the electronic structure of the 2DEG at the STO surface, as well as the interface with $LaAlO_3$ and AlO_x [11,28]. For details of this model, we refer to Refs. [11,29] and to Appendix A. In addition to atomic spin-orbit coupling, the broken inversion symmetry at the interface allows for an interatomic orbital mixing term, which leads to an effective Rashba term causing a Rashba-like spin splitting of the bands [26,27]. In order to simulate ferromagnetism originating from an adjacent ferromagnetic layer, we introduce an additional magnetic exchange coupling term to the Hamiltonian, $\mathcal{H} = \mathcal{H}_{\text{STO}} + \mathcal{H}_{\text{ex}}$, with $\mathcal{H}_{\text{STO}}$ the Hamiltonian of the unperturbed STO interface, and the exchange coupling

$$\mathcal{H}_{\text{ex}} = -\frac{J_{\text{ex}}}{\hbar}(g_l \boldsymbol{\mathcal{L}} + g_s \boldsymbol{\mathcal{S}}) \cdot \hat{\mathbf{M}}. \tag{1}$$

Here, $\hbar$ is the reduced Planck constant, $\hat{\mathbf{M}}$ is the direction of the magnetization, J_{ex} quantifies the exchange coupling between the conduction electrons' orbital/spin moments and the magnetization, and $\boldsymbol{\mathcal{L}}$ and $\boldsymbol{\mathcal{S}}$ are the operators of the orbital angular momentum and the spin, respectively, with g_l and g_s the corresponding Landé factors. The Hamiltonian (1) has the form of a Zeeman Hamiltonian [30]

$$\mathcal{H}_{\text{ex}} \widehat{=} \mathcal{H}_{\text{Z}} = \frac{\mu_{\text{B}}}{\hbar}(g_l \boldsymbol{\mathcal{L}} + g_s \boldsymbol{\mathcal{S}}) \cdot \mathbf{B}^{\text{eff}} \tag{2}$$

with μ_{B} the Bohr magneton and $\mathbf{B}^{\text{eff}} = -J_{\text{ex}}\hat{\mathbf{M}}/\mu_{\text{B}}$ an effective magnetic field originating from the finite magnetization and acting on the electronic states. The Landé factors are assumed $g_l = 1$ and $g_s = 2$, following Ref. [29]. A representation of the spin and orbital moment operators in the basis of the relevant t_{2g} orbitals can be found in Eqs. (A5)–(A7).

In the following discussion, we explore the impact of magnetic exchange coupling on the band structure and the efficiency of charge-spin conversion, in terms of the effective magnetic field B^{eff}. This field can arise either due to exchange or to proximity effects. Importantly, this field can induce an energy splitting in the band structure of a few hundred meV [31], which corresponds to a B^{eff} exceeding 1000 T. Considering STO, the anomalous Hall effect (AHE) reported for one unit cell of $La_{7/8}Sr_{1/8}MnO_3$-buffered $LaAlO_3$/STO 2DEGs with a critical temperature of approximately 30 K has been associated to Mn magnetic impurities coupled through exchange interactions mediated by electrons in the d_{xy}/d_{yz} band of STO [21]. Additionally, long-range magnetic order has been observed in EuO/STO/LSAT quantum wells, as evidenced by significant hysteresis in longitudinal magnetoresistance and AHE below 70 K corresponding to the critical temperature of EuO [32]. This follows the earlier report by Kormondy *et al.*, of a spin splitting of 0.3 eV of the d_{xy} states at the interface attributed to proximity effects [22]. In the $EuO/KTaO_3$ system, an even larger exchange splitting of 0.73 eV has been reported [33], resulting in a spin-polarized 2DEG as well as a magnetic ordering at the interface related to the occupation of $5d_{xy}$ orbitals of Ta (with 0.165 μ_{B}/Ta and perpendicular magnetic anisotropy). Such a spin splitting corresponds to a Zeeman field B^{eff} of a few thousand tesla whose influence on the band structure and charge-spin conversion is discussed below.

First, we examine the electronic band structure of the 2DEG at STO interfaces under the influence of an out-of-plane magnetic exchange field, using the model Hamiltonian introduced in Eq. (1). Figure 1 illustrates the band structure at four different out-of-plane exchange field strengths ($B_z^{\text{eff}} =$ 0, 100, 180, and 1000 T) within an energy range of −270–100 meV. For each exchange field strength, the band structure as well as isoenergy lines at three selected energies (−65, −40, and 0 meV) are shown to illustrate the influence of the exchange field on the band structure.

At zero field [Fig. 1(a)], the splitting of each band pair (marked magenta, green, orange, and blue in the right panel) is solely due to the atomic spin-orbit coupling and antisymmetric hopping (called orbital mixing in Refs. [11,28]), which lifts the twofold spin degeneracy. Close to the band edge of each band pair, the band structure is isotropic with circular isoenergy lines (① in the figure). The heavy bands' Fermi contours take the form of two perpendicular ellipses. The maximum splittings along ΓX are observed in the region from −65 to −40 meV, where avoided crossings occur, the first one between the green and orange band pairs and the second one between the magenta and green band pairs, as highlighted by the Fermi surface at −40 meV (② in the figure). In these regions, we observe a strong deviation from the simple Rashba model for free electrons.

Upon increasing the exchange field strength, we observe the expected linear increase of Zeeman-like splitting for each band pair, with the notable exception of the orange band pair that remains unsplit at Γ. To understand this band-dependent splitting caused by the exchange field, it is crucial to analyze the spin and orbital composition of the bands. By breaking the inversion symmetry at the (001) interface, the t_{2g} bands become inequivalent in energy, which is why the d_{xy} bands appear at a lower energy near the Γ point compared to the d_{yz} and d_{xz} bands. Due to SOC, states that are close in energy hybridize. In our case, the d_{yz} and d_{xz} states form the superpositions $d_{m_l=\pm1} = (-id_{yz} \mp d_{xz})/\sqrt{2}$, meaning that the cubic atomic orbitals d_{yz} and d_{xz} form the atomic orbitals $d_{m_l=\pm1}$. They are

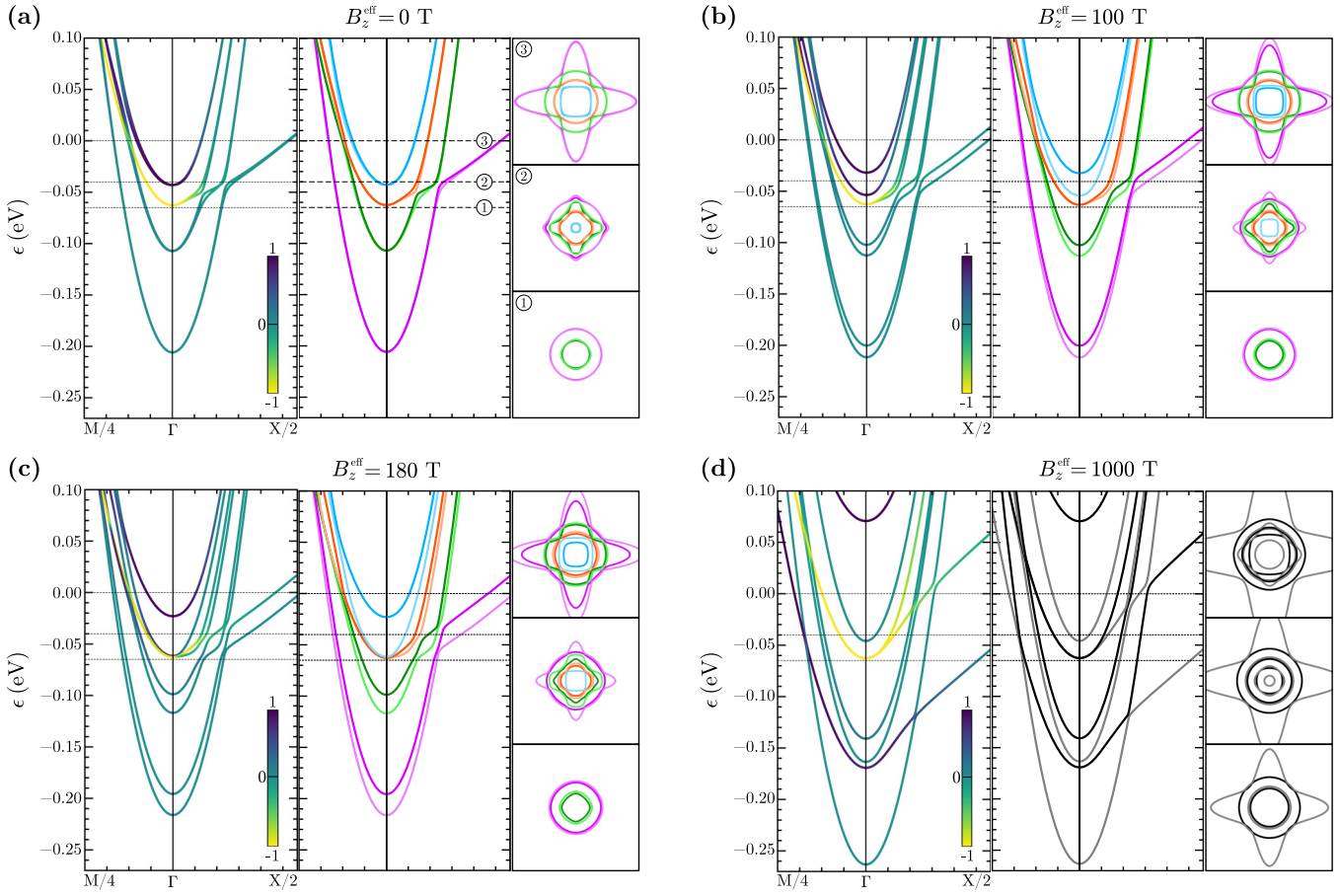

FIG. 1. Band structure and isoenergy lines of the 2DEG at STO interfaces. The band structure is computed using the tight-binding model introduced in Appendix A, for four exchange field strengths $B_z^{\rm eff} = 0\,\mathrm{T}$ (a), 100 T (b), 180 T (c), and 1000 T (d). The middle graph of each panel displays the band structure using four colors (magenta, green, orange, blue), with the lower energy bands shown in lighter shades and the higher energy bands shown in darker shades for each pair. On the right, the Fermi lines (with $|k_x|, |k_y| \leqslant \pi/2a$) illustrate the splitting of the bands for three specific energies (0, −40, and −65 meV in that order). The expectation value of the operator $\mathcal{L}_z\mathcal{S}_z$ (normalized to $\hbar^2/2$) is depicted on the left. For panel (d), the band structure and Fermi contours are displayed in black and gray due to significant intertwining of the bands, making it unreasonable to group them by pairs.

characterized by the quantum numbers $l = 2$ and $m_l = \pm 1$, with l the orbital angular momentum quantum number and m_l the quantum number of the out-of-plane orbital angular momentum operator.

The magnetic exchange field couples with both orbital angular momentum and spin [see Eq. (1)]. States with purely d_{xy}, d_{yz}, or d_{zx} character exhibit zero orbital angular momentum. However, since the t_{2g} orbitals hybridize they may possess nonzero expectation values of the out-of-plane orbital angular momentum $L_z = \hbar m_l$, because $m_l \neq 0$ as explained above. The left panel of each subfigure of Fig. 1 illustrates the spin and orbital character of the electronic states. Here, we show the expectation value of the product of out-of-plane orbital and spin operators, $\mathcal{L}_z\mathcal{S}_z$. On the colorbar: "1" means that the corresponding eigenvalues have the same sign (e.g., $m_l = 1$, $m_s = 1/2$, the parallel state), "−1" means opposite sign (e.g., $m_l = 1$, $m_s = -1/2$, the antiparallel state), and "0" means zero out-of-plane orbital quantum number (e.g., $m_l = 0$).

In the third lowest band pair (orange) spin and orbital angular momenta are antiparallel because the eigenstates are superpositions of states with opposite signs of the quantum numbers m_l and m_s ($d_{m_l=-1,m_s=1/2}$ and $d_{m_l=1,m_s=-1/2}$). In the fourth band pair (blue), they are parallel (superpositions of states with the same sign of m_l and m_s: $d_{m_l=1,m_s=1/2}$ and $d_{m_l=-1,m_s=-1/2}$). When a magnetic field is applied, the bands are polarized with respect to spin and orbital momenta. Due to the quantum numbers discussed above, the effects of the orbital- and spin-induced band splitting are compensated in the orange band pair $\Delta\epsilon = 2\mu_B(g_l\Delta L_z + g_s\Delta S_z)/\hbar \approx 0$ because $\Delta L_z \approx -2\Delta S_z$ and $g_s = 2g_l$, but are enhanced in the blue band pair $\Delta\epsilon = 2\mu_B(g_l\Delta L_z + g_s\Delta S_z)/\hbar \approx 4\mu_B|\mathbf{B}^{\rm eff}|$.

Since the lower two band pairs (magenta and green) consist of almost purely d_{xy} states at the Γ point at low magnetic fields, the orbital angular momentum L_z is suppressed for these bands, which is why they only split up due to the spin contribution: $\Delta\epsilon = 2\mu_B g_s \Delta S_z/\hbar \approx 2\mu_B|\mathbf{B}^{\rm eff}|$. These bands could only experience a considerable orbital polarization if they hybridized (a) with the orange and blue bands or (b) with $d_{x^2-y^2}$ states to form the complex orbitals $d_{m_l=\pm 2} = (d_{x^2-y^2} \pm id_{xy})/\sqrt{2}$ that are characterized by $m_l = \pm 2$.

At specific field strengths, the Zeeman-like splitting causes band crossings at Γ. This leads to increased band mixing,

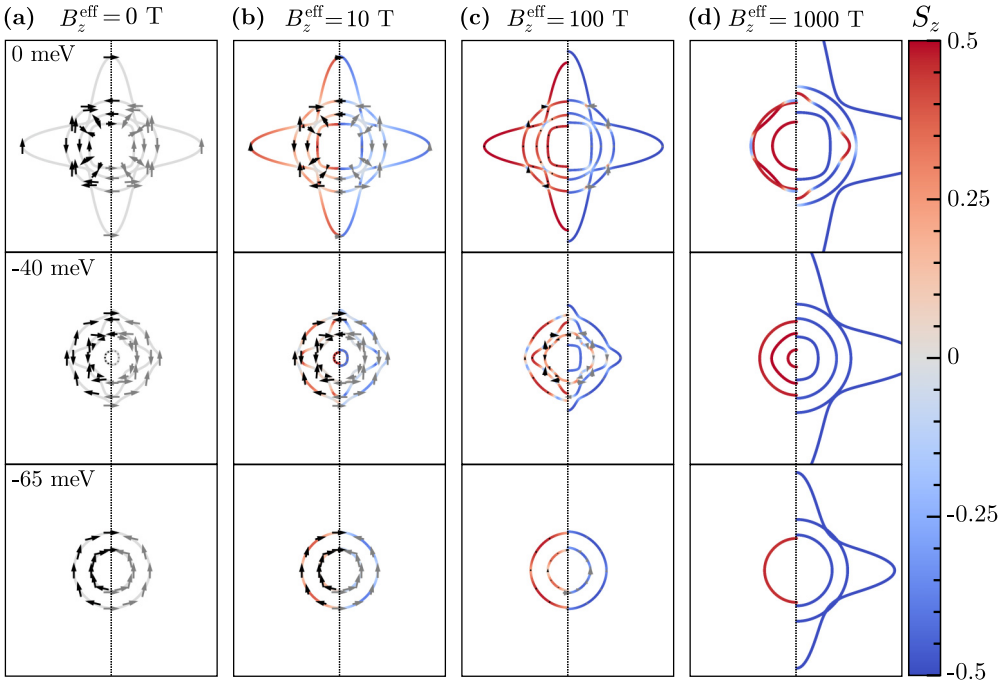

FIG. 2. Isoenergy lines and spin textures. The contour energies are the same as in Fig. 1 (0, −40, and −65 meV in that order). The exchange field strengths are different at $B_z^{\text{eff}} = 0$ T (a), 10 T (b), 100 T (c), and 1000 T (d). The arrows represent the in-plane spin expectation values, while the color indicates the out-of-plane spin expectation values. For better visibility, the left and right sides of each figure correspond to the higher energy band and lower energy band of a pair, respectively, except for 1000 T, where it corresponds to positive (resp. negative) values of S_z at Γ.

making it unreasonable to discuss them as pairs. At 190 T, the first such crossing occurs between the orange bands and lower blue band. We will explore the implications of this crossing on the spin-charge interconversion efficiency later. Thus, the center panel of Fig. 1(d) is displayed in black and gray to prevent any potential confusion regarding the concept of a band pair and its associated color representation.

To further highlight the impact of the exchange field, the spin textures at various field strengths, corresponding to the isoenergy contours depicted in Fig. 1, are presented in Fig. 2. When no out-of-plane exchange field is present [Fig. 2(a)], the spins are oriented within the plane, resulting in a zero out-of-plane spin density. The arrows in the figure, representing the in-plane spins, exhibit the familiar Rashba texture for circular contours, with the absolute values of the spin expectation values equal to $\hbar/2$. At higher energies, the spin texture becomes more intricate notably at avoided crossing points [11].

As the magnetic exchange field is increased, the in-plane spin expectation values diminish notably in favor of increased out-of-plane spin expectation values giving rise to an out-of-plane equilibrium spin magnetization of the 2DEG. This change of orientation is particularly pronounced, with the absolute out-of-plane spin expectation values (represented by the color) close to $\hbar/2$ at 1000 T [Fig. 2(d)]. More importantly, this spin reorientation would lead to a reduction of the current-induced nonequilibrium in-plane spin polarization by the Edelstein effect and to a reduction of the produced charge current by the inverse Edelstein effect when spin current is injected. Figure 2 also evidences the large impact of the field-induced Zeeman-like splitting on the bands present at the different energies and the potential of this out-of-plane field to reinforce the contrast between contours with opposite spin chiralities and thus to boost the spin-charge interconversion. The effective impact of those two counteracting effects on spin-charge interconversion is described in the next section.

III. EDELSTEIN EFFECT

The spin Edelstein effect (SEE), which is the main focus of this paper, corresponds to a nonequilibrium spin density, leading to a finite magnetization, induced by an external electric field. In order to quantify this effect, we define the spin Edelstein susceptibility χ^s:

$$\mathbf{m} = \mathbf{m}_0 + \chi^s \mathbf{E} \tag{3}$$

with $\mathbf{m}$ the total magnetic moment per unit cell, $\mathbf{m}_0$ the equilibrium magnetic moment per unit cell, and $\chi^s\mathbf{E}$ the magnetic moment originating from the current-induced spin density. The rank-2 tensor χ^s is the spin Edelstein susceptibility, and $\mathbf{E}$ is the external electric field (producing the current). However, in addition to this SEE, the electrons' orbital magnetic moments can also give rise to a finite current-induced magnetization, called the orbital Edelstein effect (OEE) [34–39]. Until recently, the experimental realization of the Edelstein effect was confined to the SEE [11,29,40,41]. It has been proposed from theory that at STO interfaces the OEE can exceed the SEE [29]. El Hamdi *et al.* then provided some indications that the OEE also contributes to the conversion [42]. We have also calculated the OEE and found that it weakly depends on the magnetic field. Since the present paper focuses on the role of magnetic field in increasing the Edelstein effect, and

because most experimental realizations are sensitive to its spin component, here we do not discuss further the OEE.

Within the semiclassical Boltzmann transport theory, the spin Edelstein susceptibility defined by Eq. (3) is given by

$$\chi^s_{ij} = g_s \frac{A_0 e \mu_B}{A\hbar} \sum_{\mathbf{k}} \tau_{\mathbf{k}} \mathbf{S}^i_{\mathbf{k}} \mathbf{v}^j_{\mathbf{k}} \delta(\epsilon_{\mathbf{k}} - \epsilon_F). \tag{4}$$

Here, A_0 is the area of the unit cell, A is the area of the sample, e is the absolute value of the elementary charge, the multi-index $\mathbf{k}$ represents the crystal momentum of an electronic state $|\mathbf{k}\rangle$ as well as the band index, $\tau_{\mathbf{k}}$ is the momentum relaxation time, which is set constant $\tau_{\mathbf{k}} = \tau_0$ in the following, $\mathbf{S}_{\mathbf{k}}$ is the spin expectation value of the state $|\mathbf{k}\rangle$, $\mathbf{v}_{\mathbf{k}}$ is the group velocity, $\epsilon_{\mathbf{k}}$ is the energy of the state $|\mathbf{k}\rangle$, and ϵ_F is the Fermi energy. We have used the relaxation time approximation to solve the linearized Boltzmann equation and assumed zero temperature. Details of the Boltzmann transport theory can be found in Appendix B.

Although the microscopic scattering processes exhibit more complexity than captured by the constant relaxation time, the constant relaxation time approximation has been found to agree qualitatively with experimental results for the inverse SEE at an AlO/STO interface [11]. In the spin-pumping experiment, which is typically used to observe the inverse SEE, electrons can scatter from the 2DEG to neighboring structures. This second scattering channel homogenizes the effective relaxation time [11]. Therefore, we chose the constant relaxation time approach here.

Further, we assume zero temperature because experimentally the charge carrier density of the 2DEG can be modified by applying a gate voltage most efficiently at low temperatures, and most experiments on spin-charge interconversion in oxide 2DEGs are performed at low temperature [10,11,42]. The influence of low, nonzero temperatures on the results is expected to be small, and to affect all results presented here qualitatively in a similar way.

The symmetry of the system allows for nonzero tensor elements $\chi^s_{xy} = -\chi^s_{yx}$, which quantify a current-induced magnetization oriented perpendicular to the applied electric field. In the presence of a nonzero magnetic exchange field, the current-induced magnetization can also exhibit a component parallel to $\mathbf{E}$ due to the broken time-reversal symmetry, represented by $\chi^s_{xx} = \chi^s_{yy}$. However, in the system under consideration, the extrinsic Edelstein effect, calculated within the Boltzmann approach, does not provide any contribution to χ^s_{xx}. This tensor element can be nonzero only due to the intrinsic Edelstein effect, calculated for example using the Kubo approach. As shown in Refs. [43,44], for a pure Rashba system with Zeeman-like splitting these intrinsic contributions to the current-induced magnetization are several orders of magnitude smaller than the extrinsic contributions as well as the equilibrium magnetization. Therefore, they are not discussed in this paper.

Figure 3 illustrates the SEE conversion efficiency as a function of the Fermi level at various exchange field strengths. The efficiency at $B_z^{\text{eff}} = 0\,\text{T}$ is depicted in red. It exhibits two positive maxima at -65 and $-15\,\text{meV}$ and a negative maximum around $-50\,\text{meV}$. The introduction of an out-of-plane exchange field notably enhances this efficiency around

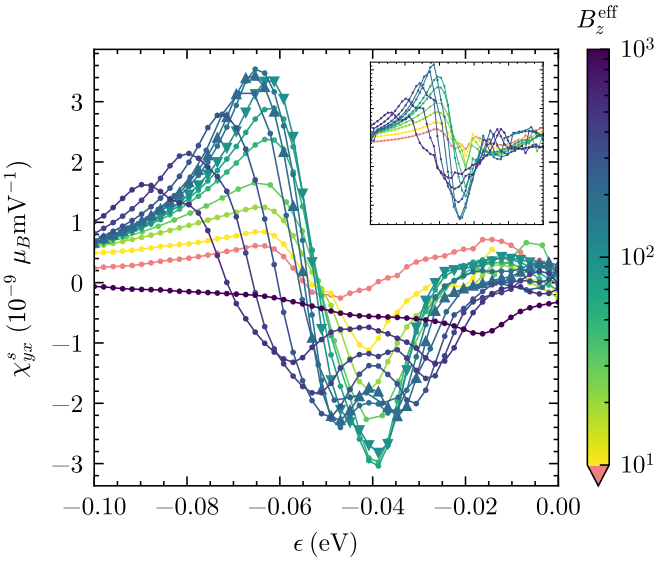

FIG. 3. Spin Edelstein effect conversion efficiency as a function of the energy at various exchange field strengths. The exchange field strengths range from 0 to 1000 T and the energy ranges from −100 to 0 meV. The conversion efficiency at zero field is represented in red. To compare with previous figures, the downward (resp. upward) pointing triangles represent 100 T (resp. 180 T). The inset corresponds to the product of average wave vector k and the average modulus of the in-plane spin expectation value of each band; for details see main text.

$-65\,\text{meV}$, by approximately an order of magnitude at 180 T; beyond this value the efficiency gradually decreases. A similar trend is observed in the -50- to -40-meV region, albeit with a negative efficiency, but the maximum is attained at a lower field (approximately 70 T). These findings highlight the significant impact of the exchange field on the SEE conversion efficiency and provide crucial insights into its optimal operating conditions. By fine tuning both B_z^{eff} and ϵ_F, a strong increase of the SEE in STO-based 2DEGs can be achieved.

To understand the strong B_z^{eff} dependence of the SEE, in particular the emergence of the maxima, we recall the Edelstein efficiency in an ordinary isotropic Rashba system [45]. For a single Rashba band pair, the Edelstein susceptibility scales with the band splitting in $\mathbf{k}$ space and the modulus of the $\mathbf{k}$ dependent in-plane spin expectation value. This relation is now transferred to the multiband STO system. The inset in Fig. 3 presents a simplified calculation based on the interplay between two competing effects: the subband splitting and the out-of-plane spin polarization. More specifically, to obtain this value, we take the energy-dependent average modulus of the wave vector k (or radius for circular contours) of each band and multiply it by the average modulus of the $\mathbf{k}$ dependent in-plane spin expectation value s^{ip}. Next, we compute the difference between the outer and inner band value of a pair. For fields higher than 190 T where the concept of "pairs" is more challenging, we pair the lowest energy band with the second lowest energy band to form the first pair (1+2), and continue in this manner until reaching the highest energy band (in the pair 7+8) [46]. Therefore we calculate $(ks^{ip})_i - (ks^{ip})_{i+1}$ with i and $i+1$ the band indices. This approach yields a result

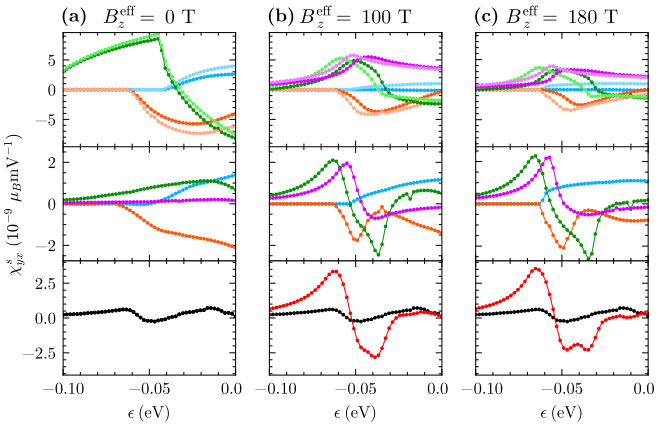

FIG. 4. Contributions to the SEE conversion efficiency at various exchange field strengths at $B_z^{\text{eff}} = 0\,\text{T}$ (a), $B_z^{\text{eff}} = 100\,\text{T}$ (b), and $B_z^{\text{eff}} = 180\,\text{T}$ (c). The top panel represents the efficiency of each band (with the contribution of the inner band multiplied by -1 for better comparison). The middle panel shows the efficiency contribution of each band pair. The bottom panel displays the total efficiency. The total efficiency at 0 T is represented in black.

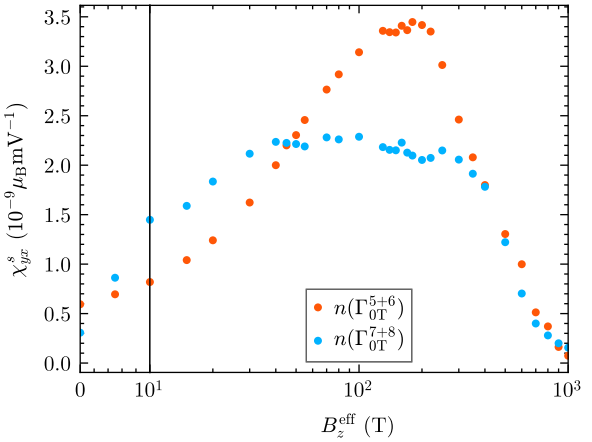

FIG. 5. Absolute value of the spin Edelstein effect conversion efficiency as a function of exchange field at constant charge carrier density. The SEE conversion efficiency is calculated at a fixed carrier density corresponding to the edge of the orange band [orange dots, $n(\Gamma_{0\,\text{T}}^{5+6}) = 5.44 \times 10^{13}\text{cm}^{-2}$ at $\epsilon = -63\,\text{meV}$] and the blue band [blue dots, $n(\Gamma_{0\,\text{T}}^{7+8}) = 8.99 \times 10^{13}\text{cm}^{-2}$ at $\epsilon = -43\,\text{meV}$] at 0 T, representing the positive and negative extrema of the efficiency at 0 T. Here, $\Gamma_{0\,\text{T}}^{5+6}$ and $\Gamma_{0\,\text{T}}^{7+8}$ correspond to the energy position of the third (orange) and fourth (blue) band pair, respectively, at the Γ point at 0 T. The scale of the abscissa is linear from 0 to 10 T and logarithmic between 10 and 1000 T.

that closely resembles the efficiency calculated within the full Boltzmann approach (Fig. 3), with a maximum value around 180 T. Hence, we conclude that the SEE provided by each band pair approximately scales with $(ks^{ip})_i - (ks^{ip})_{i+1}$. In general, large subband splitting (both in k and in s) and large absolute values of k and s^{ip} enhance the SEE. However, the multiband character of the STO-based 2DEG as well as hybridization lead to a much more intricate energy dependence of the SEE compared to a trivial Rashba system, as discussed in detail in Ref. [11] for $B_z^{\text{eff}} = 0\,\text{T}$. In particular the local extrema of the SEE shown in Fig. 3 cannot be explained using the standard Rashba model.

Figure 4 provides a decomposition of the calculated SEE efficiency. In the top panel, we observe the efficiency contributed by each individual band whereas the middle panel shows the efficiency contribution of each band pair and the bottom panel displays the total efficiency.

The energy dependence of the SEE is tied to the intricate band structure at the STO interface. At zero field and low energy, the d_{xy} bands (magenta and green) exhibit notable spin-charge conversion efficiency per band (the magenta bands are outside the range of the top panel window). Nevertheless, the pair contribution remains modest, resulting in a relatively small value of χ^s_{yx}. Upon increasing the energy, the first observed extremum corresponds to the onset at -63 meV of the first d_{yz}/d_{xz} band (orange pair) with a contribution of opposite sign to χ^s_{yx}. The SEE efficiency reaches a large negative value in the region of avoided crossing points between bands of d_{xy} and d_{yz}/d_{xz} character (-50 to -40 meV, along the $\langle 100 \rangle$ directions). The negative maximum of the efficiency is then reached at the onset (-43 meV) of the blue band, with positive contribution.

The situation becomes more intricate in the presence of an exchange field, as the contribution of each band pair displays a less monotonic behavior, with pronounced positive and negative maxima, which are related to avoided crossings. The general trend is however that, whereas the SEE efficiency value of each individual band diminishes with increasing exchange field strength because of the reduced in-plane spin expectation values, excitingly, the contributions of the band pairs and the total SEE actually increase with the field up to 180 T due to Zeeman-like splitting both in energy and $\boldsymbol{k}$, and due to modified in-plane spin expectation values.

Below the onset of the orange band, the energy dependence of the SEE is not changed qualitatively by the 100-T (180-T) exchange fields. The avoided crossing between the orange and green bands occurs around -50 meV (-60 meV), whereas the avoided crossing between green and magenta band pairs is around -45 meV (-50 meV). This region eventually coincides with the onset of the lowest blue band as they are shifted by the field, altering the negative maximum.

In the energy range around the onset of the third (orange) band pair, the two lowest (magenta and green) band pairs hybridize with the orange flat bands, which leads to pronounced maxima of the magenta and green band pairs' contributions to the SEE (see middle row of Fig. 3). The third band pair always contributes negatively to the total SEE. The coincidence of enhanced contributions from the two lowest band pairs and the onset of the negatively contributing third band pair lead to the pronounced local maximum of the SEE around -63 meV.

To further illustrate the enhancement of the efficiency due to the exchange field, we present in Fig. 5 the SEE efficiency as a function of the exchange field strength, at a constant charge carrier density [47]. As explained in Figs. 1 and 4, the edge of the orange band pair, which is the onset of the first heavy bands, remains unchanged in energy. Moreover, it coincides with the maximum efficiency, as observed in Fig. 3. Therefore, we selected the carrier density at this energy

(without exchange field; $n = 5.44 \times 10^{13}/\mathrm{cm}^2$ at $\epsilon = -63\,\mathrm{meV}$) as a reference for all field strengths.

The negative maximum of χ^s_{yx} observed around $-40\,\mathrm{meV}$ in Fig. 3 is loosely related to the edge of the blue band pair. Contrary to the orange band, its exact energy position varies with B_z^{eff}. The blue dots in Fig. 5 represent the Edelstein susceptibility for a charge carrier density of $n = 8.99 \times 10^{13}/\mathrm{cm}^2$, which corresponds to the edge of the blue band at $B_z^{\mathrm{eff}} = 0$ ($\epsilon = -43\,\mathrm{meV}$). Here, it appears that we reach a plateau instead of a distinct peak. As emphasized in Fig. 4, the negative maximum does not correspond to a well-defined peak.

The presence of an out-of-plane magnetic exchange field generally enhances the splitting of each band pair in terms of wave vector (k) and spin expectation values (s). It also tilts the spin expectation values out of the plane, thereby reducing their in-plane components. Regarding the Edelstein conversion efficiency, these two effects compete with each other. Surprisingly, the nonmonotonic behavior of the spin Edelstein susceptibility as a function of B_z^{eff}, shown in Fig. 5, is dominated by the difference in in-plane spin expectation values ($s_i^{ip} - s_{i+1}^{ip}$), and not by the increased splitting in k space or the reduced in-plane spin expectation values. The same quantity also determines the B_z^{eff} dependence of the SEE in a pure Rashba system, which, however, exhibits no pronounced maximum, but increases with B_z^{eff} until reaching a plateau value. Hence, for the STO-based multiband 2DEG, no simple relation between the effective Rashba SOC, the magnetic exchange field, and the maximum of the SEE exists. Rather, the strong enhancement of the SEE by nearly one order of magnitude for $B_z^{\mathrm{eff}} = 180\,\mathrm{T}$ compared to the maximum SEE without a field is a consequence of hybridization leading to avoided crossings, and the magnetic exchange field rearranging the bands.

IV. CONCLUSION

In conclusion, this paper sheds light on the influence of a perpendicular exchange field on the spin-charge interconversion in the Rashba 2DEG at $SrTiO_3$ interfaces. Remarkably, increasing the magnetic field yields an up to sixfold increase of the spin-charge interconversion efficiency which we explain by the competing exchange and Rashba interactions. We have found that an out-of-plane magnetic field produces a Zeeman splitting of the band pairs both in k and s, thereby increasing the Edelstein effect. At the same time, it strongly modifies the Rashba-type spin textures and tilts them from their original in-plane direction towards an out-of-plane direction, thereby reducing the Edelstein effect. Therefore, a tradeoff of the two competing effects causes a maximum which we observe close to a field strength of 190 T, which is where shifted bands overlap close to the Γ point.

Our findings open routes to provide more efficient SOC materials or interfaces for emerging devices such as the MESO device proposed by Intel [12]. They are also relevant because several studies have reported STO 2DEGs at interfaces with a magnetic oxide such as $EuTiO_3$ [20], EuO [48], or LSMO [49], with indications of induced magnetism in the 2DEG [20,25,49]. Finally, our results suggest a general approach that could be tested on other Rashba systems endowed with magnetic interactions, such as $PdCoO_2$ interface/surface states [50], $EuO/KTaO_3$ [51], or certain van der Waals heterostructures [52].

ACKNOWLEDGMENTS

This work received support from European Research Council AdG "FRESCO" Grant No. 833973. This work is supported by CRC/TRR 227 of Deutsche Forschungsgemeinschaft (DFG).

APPENDIX A: TIGHT-BINDING MODEL FOR STO-BASED 2DEGS

Following Refs. [11,26–29], we describe the electronic states which are relevant for the formation of the 2DEG at STO interfaces by an effective tight-binding Hamiltonian $\mathcal{H}_{\mathrm{STO}}$ in the basis set $(d^{(1)}_{xy\uparrow}, d^{(2)}_{xy\uparrow}, d_{yz\uparrow}, d_{zx\uparrow}, d^{(1)}_{xy\downarrow}, d^{(2)}_{xy\downarrow}, d_{yz\downarrow}, d_{zx\downarrow})$. Two d_{xy} orbitals occur due to the confinement of the 2DEG along the z direction. The full Hamiltonian $\mathcal{H}_{\mathrm{STO}}$ can be split into three terms:

$$\mathcal{H}_{\mathrm{STO}} = \mathcal{H}_0 + \mathcal{H}_\lambda + \mathcal{H}_{\mathrm{OM}}. \tag{A1}$$

Here, $\mathcal{H}_0$ is the free-electron-like Hamiltonian neglecting spin-orbit coupling:

$$\mathcal{H}_0 = \mathbb{1} \otimes \begin{pmatrix} \epsilon^{(1)}_{xy} & 0 & 0 & 0 \\ 0 & \epsilon^{(2)}_{xy} & 0 & 0 \\ 0 & 0 & \epsilon_{yz} & 0 \\ 0 & 0 & 0 & \epsilon_{zx} \end{pmatrix} \tag{A2}$$

with

$$\begin{aligned} \epsilon^{(i)}_{xy} &= 2t(2 - \cos ak_x - \cos ak_y) + \epsilon^{(i)}_{xy0}, \quad i = 1, 2, \\ \epsilon_{yz} &= 2t(1 - \cos ak_y) + 2t_h(1 - \cos ak_x) + \epsilon_{z0}, \\ \epsilon_{zx} &= 2t(1 - \cos ak_x) + 2t_h(1 - \cos ak_y) + \epsilon_{z0}. \end{aligned} \tag{A3}$$

Here, $\mathbf{k}$ is the crystal momentum, a is the lattice constant, the parameters t and t_h describe nearest-neighbor hopping of the light and heavy bands, respectively, and $\epsilon_{xy0/z0}$ correspond to the on-site potentials.

The second term of the right-hand side of Eq. (A1) corresponds to atomic spin-orbit coupling:

$$\mathcal{H}_\lambda = \frac{2}{\hbar^2}\lambda \boldsymbol{\mathcal{L}} \cdot \boldsymbol{\mathcal{S}}, \tag{A4}$$

with $\boldsymbol{\mathcal{L}}$ and $\boldsymbol{\mathcal{S}}$ the orbital angular momentum and spin operators, respectively, which are represented in our particular basis set as

$$\mathcal{L}_i = \hbar \mathbb{1} \otimes l_i, \quad i = x, y, z \tag{A5}$$

with

$$l_x = \begin{pmatrix} 0 & 0 & 0 & -i \\ 0 & 0 & 0 & -i \\ 0 & 0 & 0 & 0 \\ i & i & 0 & 0 \end{pmatrix}, \quad l_y = \begin{pmatrix} 0 & 0 & i & 0 \\ 0 & 0 & i & 0 \\ -i & -i & 0 & 0 \\ 0 & 0 & 0 & 0 \end{pmatrix}, \quad l_z = \begin{pmatrix} 0 & 0 & 0 & 0 \\ 0 & 0 & 0 & 0 \\ 0 & 0 & 0 & i \\ 0 & 0 & -i & 0 \end{pmatrix}, \tag{A6}$$

and

$$\mathcal{S}_i = \frac{\hbar}{2}\sigma_i \otimes \mathbb{1} \tag{A7}$$

with σ_i the Pauli spin matrices. Finally, the term $\mathcal{H}_{\mathrm{OM}}$ in Eq. (A1) corresponds to interatomic orbital mixing, arising from the broken inversion symmetry at the interface leading to a deformation of the orbitals [26,27,53]:

$$\mathcal{H}_{\mathrm{OM}} = \mathbb{1} \otimes \begin{pmatrix} 0 & 0 & 2ig_1 \sin ak_x & 2ig_1 \sin ak_y \\ 0 & 0 & 2ig_2 \sin ak_x & 2ig_2 \sin ak_y \\ -2ig_1 \sin ak_x & -2ig_2 \sin ak_x & 0 & 0 \\ -2ig_1 \sin ak_y & -2ig_2 \sin ak_y & 0 & 0 \end{pmatrix}. \tag{A8}$$

In this paper, we use the following parameters, adopted from Refs. [11,28]:

$$\epsilon^{(1)}_{xy0} = -205\,\mathrm{meV}, \quad t = 388\,\mathrm{meV}, \quad \epsilon^{(2)}_{xy0} = -105\,\mathrm{meV}, \quad t_h = 31\,\mathrm{meV},$$
$$\epsilon_{z0} = -54\,\mathrm{meV}, \quad g_1 = 2\,\mathrm{meV}, \quad \lambda = -8.3\,\mathrm{meV}, \quad g_2 = 5\,\mathrm{meV}. \tag{A9}$$

APPENDIX B: BOLTZMANN TRANSPORT THEORY

Within the semiclassical Boltzmann transport theory, the current-induced magnetic moment per unit cell originating from the spin Edelstein effect is given by

$$\mathbf{m} = -\frac{A_0 g_s \mu_{\mathrm{B}}}{A\hbar} \sum_{\mathbf{k}} f_{\mathbf{k}} \mathbf{S}_{\mathbf{k}}, \tag{B1}$$

with A_0 the area of the unit cell, A the area of the sample, and $f_{\mathbf{k}}$ the distribution function, which is split into an equilibrium part, the Fermi-Dirac distribution function $f^0_{\mathbf{k}}$, and a nonequilibrium part $g_{\mathbf{k}}$.

In magnetic systems, the term of Eq. (B1) containing $f^0_{\mathbf{k}}$ gives rise to an equilibrium magnetization $\mathbf{m}_0$. In the STO-based 2DEG discussed in this paper, the magnetic exchange field B^z_{eff} induces a finite out-of-plane equilibrium magnetization. The application of an external electric field $\mathbf{E}$ leads to a change of the distribution function, represented by $g_{\mathbf{k}}$, whose contribution to Eq. (B1) is a current-induced nonequilibrium magnetic moment, the Edelstein effect.

The nonequilibrium distribution function $g_{\mathbf{k}}$ is determined by solving the Boltzmann equation. Here, we consider a spatially homogeneous and stationary system:

$$\dot{\mathbf{k}} \frac{\partial f_{\mathbf{k}}}{\partial \mathbf{k}} = \left(\frac{\partial f_{\mathbf{k}}}{\partial t}\right)_{\mathrm{scatt}}. \tag{B2}$$

In the presence of an external electric field, the semiclassical equation of motion reads

$$\dot{\mathbf{k}} = -\frac{e}{\hbar}\mathbf{E}. \tag{B3}$$

Within the relaxation time approximation, the scattering term is expressed by

$$\left(\frac{\partial f_{\mathbf{k}}}{\partial t}\right)_{\mathrm{scatt}} = -\frac{1}{\tau_{\mathbf{k}}} g_{\mathbf{k}} \tag{B4}$$

with $\tau_{\mathbf{k}}$ the relaxation time, which is assumed constant, $\tau_{\mathbf{k}} = \tau_0$ in our calculations.

The Boltzmann equation (B2) is then solved by

$$f_{\mathbf{k}} = f^0_{\mathbf{k}} + \frac{\partial f_{\mathbf{k}}}{\partial \epsilon} e\tau_0 \mathbf{v}_{\mathbf{k}} \cdot \mathbf{E}. \tag{B5}$$

Inserting this solution into Eq. (B1) and assuming zero temperature, Eq. (3) for the Edelstein susceptibility, characterizing the nonequilibrium current-induced magnetic moment, is obtained.

[1] A. Ohtomo and H. Y. Hwang, A high-mobility electron gas at the $LaAlO_3/SrTiO_3$ heterointerface, Nature (London) **427**, 423 (2004).

[2] N. Reyren, S. Thiel, A. D. Caviglia, L. F. Kourkoutis, G. Hammerl, C. Richter, C. W. Schneider, T. Kopp, A.-S. Rüetschi, D. Jaccard, M. Gabay, D. A. Muller, J.-M. Triscone, and J. Mannhart, Superconducting interfaces between insulating oxides, Science **317**, 1196 (2007).

[3] A. Brinkman, M. Huijben, M. van Zalk, J. Huijben, U. Zeitler, J. C. Maan, W. G. van der Wiel, G. Rijnders, D. H. A. Blank, and H. Hilgenkamp, Magnetic effects at the interface between non-magnetic oxides, Nat. Mater. **6**, 493 (2007).

[4] L. Li, C. Richter, J. Mannhart, and R. C. Ashoori, Coexistence of magnetic order and two-dimensional superconductivity at $LaAlO_3/SrTiO_3$ interfaces, Nat. Phys. **7**, 762 (2011).

[5] S. Thiel, G. Hammerl, A. Schmehl, C. W. Schneider, and J. Mannhart, Tunable quasi-two-dimensional electron gases in oxide heterostructures, Science **313**, 1942 (2006).

[6] A. D. Caviglia, S. Gariglio, N. Reyren, D. Jaccard, T. Schneider, M. Gabay, S. Thiel, G. Hammerl, J. Mannhart, and J.-M. Triscone, Electric field control of the $LaAlO_3/SrTiO_3$ interface ground state, Nature (London) **456**, 624 (2008).

[7] A. D. Caviglia, M. Gabay, S. Gariglio, N. Reyren, C. Cancellieri, and J.-M. Triscone, Tunable Rashba spin-orbit interaction at oxide interfaces, Phys. Rev. Lett. **104**, 126803 (2010).

[8] C. Cen, S. Thiel, J. Mannhart, and J. Levy, Oxide nanoelectronics on demand, Science **323**, 1026 (2009).

[9] L. Kornblum, Conductive oxide interfaces for field effect devices, Adv. Mater. Interfaces **6**, 1900480 (2019).

[10] E. Lesne, Y. Fu, S. Oyarzun, J. C. Rojas-SÃ¡nchez, D. C. Vaz, H. Naganuma, G. Sicoli, J.-P. Attané, M. Jamet, E. Jacquet, J.-M. George, A. Barthélémy, H. Jaffrès, A. Fert, M. Bibes, and L. Vila, Highly efficient and tunable spin-to-charge conversion through Rashba coupling at oxide interfaces, Nat. Mater. **15**, 1261 (2016).

[11] D. C. Vaz, P. Noël, A. Johansson, B. Göbel, F. Y. Bruno, G. Singh, S. McKeown-Walker, F. Trier, L. M. Vicente-Arche, A. Sander, S. Valencia, P. Bruneel, M. Vivek, M. Gabay, N. Bergeal, F. Baumberger, H. Okuno, A. Barthélémy, A. Fert, L. Vila *et al.*, Mapping spin-charge conversion to the band structure in a topological oxide two-dimensional electron gas, Nat. Mater. **18**, 1187 (2019).

[12] S. Manipatruni, D. E. Nikonov, C.-C. Lin, T. A. Gosavi, H. Liu, B. Prasad, Y.-L. Huang, E. Bonturim, R. Ramesh, and I. A. Young, Scalable energy-efficient magnetoelectric spin-orbit logic, Nature (London) **565**, 35 (2019).

[13] D. C. Vaz *et al.*, Voltage-based magnetization switching and reading in magnetoelectric spin-orbit nanodevices, arXiv:2302.12162.

[14] F. Trier, P. Noël, J.-V. Kim, J.-P. Attané, L. Vila, and M. Bibes, Oxide spin-orbitronics: Spin-charge interconversion and topological spin textures, Nat. Rev. Mater. **7**, 258 (2022).

[15] F. Gallego, F. Trier, S. Mallik, J. Bréhin, S. Varotto, L. Moreno Vicente-Arche, T. Gosavy, C.-C. Lin, J.-R. Coudevylle, L. Iglesias, F. Casanova, I. Young, L. Vila, J.-P. Attané, and M. Bibes, All-electrical detection of the spin-charge conversion in nanodevices based on $SrTiO_3$ 2-D electron gases, Adv. Funct. Mater. **34**, 2307474 (2023).

[16] P. Noël, F. Trier, L. M. Vicente Arche, J. Bréhin, D. C. Vaz, V. Garcia, S. Fusil, A. Barthélémy, L. Vila, M. Bibes, and J.-P. Attané, Non-volatile electric control of spin-charge conversion in a $SrTiO_3$ Rashba system, Nature (London) **580**, 483 (2020).

[17] J. Bréhin, F. Trier, L. M. Vicente-Arche, P. Hemme, P. Noël, M. Cosset-Chéneau, J.-P. Attané, L. Vila, A. Sander, Y. Gallais, A. Sacuto, B. Dkhil, V. Garcia, S. Fusil, A. Barthélémy, M. Cazayous, and M. Bibes, Switchable two-dimensional electron gas based on ferroelectric $Ca:SrTiO_3$, Phys. Rev. Mater. **4**, 041002(R) (2020).

[18] G. M. De Luca, R. Di Capua, E. Di Gennaro, F. M. Granozio, D. Stornaiuolo, M. Salluzzo, A. Gadaleta, I. Pallecchi, D. Marrè, C. Piamonteze, M. Radovic, Z. Ristic, and S. Rusponi, Transport properties of a quasi-two-dimensional electron system formed in $LaAlO_3/EuTiO_3/SrTiO_3$ heterostructures, Phys. Rev. B **89**, 224413 (2014).

[19] F. Gunkel, C. Bell, H. Inoue, B. Kim, A. G. Swartz, T. A. Merz, Y. Hikita, S. Harashima, H. K. Sato, M. Minohara, S. Hoffmann-Eifert, R. Dittmann, and H. Y. Hwang, Defect control of conventional and anomalous electron transport at complex oxide interfaces, Phys. Rev. X **6**, 031035 (2016).

[20] D. Stornaiuolo, C. Cantoni, G. M. De Luca, R. Di Capua, E. Di Gennaro, G. Ghiringhelli, B. Jouault, D. Marrè, D. Massarotti, F. Miletto Granozio, I. Pallecchi, C. Piamonteze, S. Rusponi, F. Tafuri, and M. Salluzzo, Tunable spin polarization and superconductivity in engineered oxide interfaces, Nat. Mater. **15**, 278 (2016).

[21] H. R. Zhang, Y. Zhang, H. Zhang, J. Zhang, X. Shen, X. X. Guan, Y. Z. Chen, R. C. Yu, N. Pryds, Y. S. Chen, B. G. Shen, and J. R. Sun, Magnetic two-dimensional electron gas at the manganite-buffered $LaAlO_3/SrTiO_3$ interface, Phys. Rev. B **96**, 195167 (2017).

[22] K. J. Kormondy, L. Gao, X. Li, S. Lu, A. B. Posadas, S. Shen, M. Tsoi, M. R. McCartney, D. J. Smith, J. Zhou, L. L. Lev, M.-A. Husanu, V. N. Strocov, and A. A. Demkov, Large positive linear magnetoresistance in the two-dimensional t_{2g} electron gas at the $EuO/SrTiO_3$ interface, Sci. Rep. **8**, 7721 (2018).

[23] Y. Gan, D. V. Christensen, Y. Zhang, H. Zhang, D. Krishnan, Z. Zhong, W. Niu, D. J. Carrad, K. Norrman, M. von Soosten, T. S. Jespersen, B. Shen, N. Gauquelin, J. Verbeeck, J. Sun, N. Pryds, and Y. Chen, Diluted oxide interfaces with tunable ground states, Adv. Mater. **31**, 1805970 (2019).

[24] R. Di Capua, M. Verma, M. Radovic, V. N. Strocov, C. Piamonteze, E. B. Guedes, N. C. Plumb, Y. Chen, M. DAntuono, G. M. De Luca, E. Di Gennaro, D. Stornaiuolo, D. Preziosi, B. Jouault, F. Miletto Granozio, A. Sambri, R. Pentcheva, G. Ghiringhelli, and M. Salluzzo, Orbital selective switching of ferromagnetism in an oxide quasi two-dimensional electron gas, npj Quantum Mater. **7**, 41 (2022).

[25] J. Bréhin, Y. Chen, M. DAntuono, S. Varotto, D. Stornaiuolo, C. Piamonteze, J. Varignon, M. Salluzzo, and M. Bibes, Coexistence and coupling of ferroelectricity and magnetism in an oxide two-dimensional electron gas, Nat. Phys. **19**, 823 (2023).

[26] G. Khalsa, B. Lee, and A. H. MacDonald, Theory of t_{2g} electron-gas Rashba interactions, Phys. Rev. B **88**, 041302(R) (2013).

[27] Z. Zhong, A. Tóth, and K. Held, Theory of spin-orbit coupling at $LaAlO_3/SrTiO_3$ interfaces and $SrTiO_3$ surfaces, Phys. Rev. B **87**, 161102(R) (2013).

[28] M. Vivek, M. O. Goerbig, and M. Gabay, Topological states at the (001) surface of $SrTiO_3$, Phys. Rev. B **95**, 165117 (2017).

[29] A. Johansson, B. Göbel, J. Henk, M. Bibes, and I. Mertig, Spin and orbital Edelstein effects in a two-dimensional electron gas: Theory and application to $SrTiO_3$ interfaces, Phys. Rev. Res. **3**, 013275 (2021).

[30] A. Manchon and S. Zhang, Theory of spin torque due to spin-orbit coupling, Phys. Rev. B **79**, 094422 (2009).

[31] J. Krempaský, S. Muff, F. Bisti, M. Fanciulli, H. Volfová, A. P. Weber, N. Pilet, P. Warnicke, H. Ebert, J. Braun, F. Bertran, V. V. Volobuev, J. Minár, G. Springholz, J. H. Dil, and V. N. Strocov, Entanglement and manipulation of the magnetic and

spin-orbit order in multiferroic Rashba semiconductors, Nat. Commun. **7**, 13071 (2016).

[32] J. Zhang, H. Zhang, H. Zhang, Y. Ma, X. Chen, F. Meng, S. Qi, Y. Chen, F. Hu, Q. Zhang, B. Liu, B. Shen, W. Zhao, W. Han, and J. Sun, Long-range magnetic order in oxide quantum wells hosting two-dimensional electron gases, ACS Appl. Mater. Interfaces **12**, 28775 (2020).

[33] S. Kakkar and C. Bera, Non-trivial topological states in spin-polarized 2D electron gas at EuO-KTO interface with the Rashba spin texture, Adv. Phys. Res. **2**, 2200026 (2023).

[34] L. S. Levitov, Y. V. Nazarov, and G. M. Éliashberg, Magnetoelectric effects inconductors with mirror isomer symmetry, Zh. Eksp. Teor. Fiz. **88**, 229 (1985) [Sov. Phys. JETP **61**, 133 (1985)].

[35] T. Koretsune, R. Arita, and H. Aoki, Magneto-orbital effect without spin-orbit interactions in a noncentrosymmetric zeolite-templated carbon structure, Phys. Rev. B **86**, 125207 (2012).

[36] T. Yoda, T. Yokoyama, and S. Murakami, Current-induced orbital and spin magnetizations in crystals with helical structure, Sci. Rep. **5**, 12024 (2015).

[37] D. Go, J.-P. Hanke, P. M. Buhl, F. Freimuth, G. Bihlmayer, H.-W. Lee, Y. Mokrousov, and S. Blügel, Toward surface orbitronics: Giant orbital magnetism from the orbital Rashba effect at the surface of *sp*-metals, Sci. Rep. **7**, 46742 (2017).

[38] L. Salemi, M. Berritta, A. K. Nandy, and P. M. Oppeneer, Orbitally dominated Rashba-Edelstein effect in noncentrosymmetric antiferromagnets, Nat. Commun. **10**, 5381 (2019).

[39] D. Hara, M. S. Bahramy, and S. Murakami, Current-induced orbital magnetization in systems without inversion symmetry, Phys. Rev. B **102**, 184404 (2020).

[40] J. C. Rojas Sánchez, L. Vila, G. Desfonds, S. Gambarelli, J. P. Attané, J. M. De Teresa, C. Magén, and A. Fert, Spin-to-charge conversion using Rashba coupling at the interface between non-magnetic materials, Nat. Commun. **4**, 2944 (2013).

[41] J.-C. Rojas-Sánchez, S. Oyarzún, Y. Fu, A. Marty, C. Vergnaud, S. Gambarelli, L. Vila, M. Jamet, Y. Ohtsubo, A. Taleb-Ibrahimi, P. Le Fèvre, F. Bertran, N. Reyren, J.-M. George, and A. Fert, Spin to charge conversion at room temperature by spin pumping into a new type of topological insulator: α-Sn films, Phys. Rev. Lett. **116**, 096602 (2016).

[42] A. El Hamdi, J.-Y. Chauleau, M. Boselli, C. Thibault, C. Gorini, A. Smogunov, C. Barreteau, S. Gariglio, J.-M. Triscone, and M. Viret, Observation of the orbital inverse Rashba-Edelstein effect, Nat. Phys. **19**, 1855 (2023).

[43] A. Dyrdał, J. Barnaś, and V. K. Dugaev, Current-induced spin polarization of a magnetized two-dimensional electron gas with Rashba spin-orbit interaction, Phys. Rev. B **95**, 245302 (2017).

[44] A. Johansson, Spin-orbit driven transport: Edelstein effect and chiral anomaly, Ph.D. thesis, Martin-Luther-Universität Halle-Wittenberg, 2019.

[45] V. M. Edelstein, Spin polarization of conduction electrons induced by electric current in two-dimensional asymmetric electron systems, Solid State Commun. **73**, 233 (1990).

[46] Note that this classification of bands affects only the approximated curve (inset) but not the accurate calculation of the Edelstein effect (main figure) based on Eq. (4).

[47] Note that the shift of the bands caused by the exchange field alters the density of states and therefore effectively shifts the location of the Fermi energy. To compare the Edelstein signals for different field strengths it is more significant to compare configurations with equal carrier density than equal energy.

[48] P. Lömker, T. C. Rödel, T. Gerber, F. Fortuna, E. Frantzeskakis, P. Le Fèvre, F. Bertran, M. Müller, and A. F. Santander-Syro, Two-dimensional electron system at the magnetically tunable EuO/$SrTiO_3$ interface, Phys. Rev. Mater. **1**, 062001(R) (2017).

[49] W. M. Lü, S. Saha, X. R. Wang, Z. Q. Liu, K. Gopinadhan, A. Annadi, S. W. Zeng, Z. Huang, B. C. Bao, C. X. Cong, M. Venkatesan, T. Yu, J. M. D. Coey, Ariando, and T. Venkatesan, Long-range magnetic coupling across a polar insulating layer, Nat. Commun. **7**, 11015 (2016).

[50] J. H. Lee, T. Harada, F. Trier, L. Marcano, F. Godel, S. Valencia, A. Tsukazaki, and M. Bibes, Nonreciprocal transport in a Rashba ferromagnet, delafossite $PdCoO_2$, Nano Lett. **21**, 8687 (2021).

[51] H. Zhang, Y. Yun, X. Zhang, H. Zhang, Y. Ma, X. Yan, F. Wang, G. Li, R. Li, T. Khan, Y. Chen, W. Liu, F. Hu, B. Liu, B. Shen, W. Han, and J. Sun, High-mobility spin-polarized two-dimensional electron gases at EuO/$KTaO_3$ interfaces, Phys. Rev. Lett. **121**, 116803 (2018).

[52] S. Shi, X. Wang, Y. Zhao, and W. Zhao, Recent progress in strong spin-orbit coupling van der Waals materials and their heterostructures for spintronic applications, Mater. Today Elec. **6**, 100060 (2023).

[53] L. Petersen and P. Hedegård, A simple tight-binding model of spin-orbit splitting of *sp*-derived surface states, Surf. Sci. **459**, 49 (2000).